Zacherl and Baumann *Geothermal Energy* (2023) 11:11
https://doi.org/10.1186/s40517-023-00256-4

Geothermal Energy

RESEARCH Open Access

Quantification of the effect of gas–water–equilibria on carbonate precipitation

Lilly Zacherl[1] and Thomas Baumann[1*]

*Correspondence:
tbaumann@tum.de

[1] TUM School of Engineering and Design, Chair of Hydrogeology, Technical University of Munich, Arcisstr. 21, 80333 Munich, Germany

Abstract

The expanding geothermal energy sector still faces performance issues due to scalings in pipes and surface level installations, which require elevated operation pressure levels and costly maintenance. For facilities in the North Alpine Foreland Basin, the precipitation of $CaCO_3$ is the main problem which is a consequence of the disruption of the lime-carbonic acid equilibrium during production. The formation of gas bubbles plays a key role in the scaling process. This work presents experiments in a bubble column to quantify the effects of gas stripping on carbonate precipitation and an extension of PhreeqC to include kinetic exchange between a gas phase and water for the simulation of the experimental results. With the same hybrid model not only precipitation of $CaCO_3$ but also the dissolution of scalings by the injection of CO_2 could be quantified. The bubble column was filled with tap water and brine. By varying the ionic strength of the solution, a wider range of geothermal waters was covered. Air and CO_2 were introduced at the bottom. The precipitates built on the column wall were analyzed with Raman spectroscopy: injecting air into tap water at low ionic strength led to the formation of aragonite with 59.8% of the precipitates remaining at the column wall and the rest as particles in dispersion. At moderate ionic strength the dominant polymorph was calcite and 81.5% of the crystals were attached to the wall. At high ionic strength precipitation was inhibited. The presence of crystallization nuclei reduced the time for precipitation, but not the amount of scalings formed. Injecting CO_2 into the solution completely removed the scalings from the column wall. The model and its experimental backup lay the foundation for a process-based prediction of the scales (not only) in geothermal systems.

Keywords: Scalings, Geothermal, Degassing, PhreeqC, Lime carbonic acid equilibrium

Introduction

The disruption of hydrochemical equilibria along the geothermal cycle forces geothermal facilities to deal with performance issues and unexpected down-times leading to technical and economical losses in efficiency. While the North Alpine Foreland Basin (NAFB) is one of the most promising regions to explore deep hydrogeothermal energy (Weber et al. 2016; Eyerer et al. 2017), the waters present in the sediments of the Upper Jurassic limestones and dolomites are also vulnerable to a disruption of the lime-carbonic acid equilibrium which leads to the formation of scalings (mostly $CaCO_3$ precipitation) in pipes and plants (Köhl et al. 2020; Wanner et al. 2017).

Based on gas inclusions in scalings, it was suggested that the development of a free gas phase causes stripping of CO_2 and that boiling is the most plausible mechanism to generate the gas phase (Wanner et al. 2017). However, from a mechanistic point of view, the presence of gas inclusions in scalings only proves that a gas phase was present during a very fast precipitation event. Whether the gas phase was driving the scaling process or not depends on the total disruption of the equilibrium due to stripping effects. The assumption that boiling water is the main cause for CO_2-stripping (Wanner et al. 2017), seems not justified. Previous and recent studies show that the water in the NAFB can contain high concentrations of dissolved gases, mostly N_2, CH_4, C_2H_6. The bubble point of the geothermal waters at many facilities is above 1000 to 1200 kPa while the vapor pressure of water at temperatures up to 150 °C is below 470 kPa. Hence, more likely the driving force is stripping by other gases (Mayrhofer et al. 2013; Köhl et al. 2020).

The lime-carbonic acid equilibrium (see Eqs. 1–3) depends on the pressure, temperature, and the pH-value of the system (Appelo and Postma 2005):

$$CaCO_3 + H_2CO_3^* \rightleftharpoons Ca^{2+} + 2HCO_3^- \tag{1}$$

$$CaCO_3 + H^+ \rightleftharpoons Ca^{2+} + HCO_3^- \tag{2}$$

$$CaCO_3 + H_2O \rightleftharpoons Ca^{2+} + HCO_3^- + OH^- \tag{3}$$

Here, $H_2CO_3^*$ is the sum of dissolved CO_2 ($CO_{2(aq)}$) and carbonic acid (H_2CO_3). The equilibrium is heavily shifted towards $CO_{2(aq)}$, at 25 °C only 0.2% of $H_2CO_3^*$ is dissolved carbonic acid. The concentration of dissolved CO_2 and the partial pressure of CO_2 are related through the Henry constant (Sander 2015). Thus, a change of the CO_2 partial pressure has a direct effect on the equilibrium.

The reaction rate of the dissolution of calcite is (Plummer et al. 1978):

$$r = k_1 \cdot [H^+] + k_2 \cdot [H_2CO_3] + k_3 \cdot [H_2O] - k_4 \cdot [Ca^{2+}][HCO_3^-] \tag{4}$$

with the reaction rate r and the rate constants k_1 - k_4, which represent the influence of the following aspects: k_1 the pH value, k_2 the partial pressure of CO_2, k_3 the activity of water and k_4 the reverse reaction (precipitation of calcite, depends on the concentration of Ca^{2+} and HCO_3^-). In a closed system, a decreasing CO_2 partial pressure shifts the equilibrium to higher pH-values and higher saturation (Gal et al. 2002a, b; Lipus and Dobersek 2007). This frequently happens if gas bubbles are formed in the system. According to Henry's law (1803), as soon as gas bubbles are formed, the gas phase has to fully equilibrate with the dissolved gases in the water phase. Thus, a net mass transfer of CO_2 from the water phase into the bubbles takes place. This stripping influences the lime-carbonic acid equilibrium and promotes scaling by increasing the pH of the solution. Considering the size of gas bubbles in such systems, the assumption of equal concentrations in the gas phase is justified. At turbulent flow conditions, diffusion in the water phase becomes negligible and a constant gradient between water and gas is a good approximation allowing to calculate the stripping effect. Likewise, increasing the CO_2 partial pressure, i.e. by injection of CO_2, shifts the equilibrium to lower pH-values and

the system becomes less saturated. This has been used to prevent carbonate scalings in, e.g., heat storage applications (Ueckert and Baumann 2019).

While the general processes of scale formation processes are well understood (Köhl et al. 2020; Schröder and Hesshaus 2009; Ueckert et al. 2020; Chang et al. 2017), the quantitative prediction of scales in technical systems is still not reliable enough for predictive maintenance. Part of this uncertainty is caused by a poor quantification of scale kinetics due to a simultaneous change of concentrations, gas phases, pressure, and temperature. Current investigations (e.g., Köhl et al. 2020; Wanner et al. 2017) are site specific and can be extrapolated only with the respective calibration data set. They use the saturation index (SI) of $CaCO_3$ ($SI = \log \frac{IAP}{K_{sp}}$, with the ion activity product, IAP, of the ion activities of Ca^{2+} and $CO_3{}^{2-}$ and the solubility product of $CaCO_3$, K_{sp} (Appelo and Postma 2005)) as a proxy to describe the development of scalings. At this stage, the results are perfect to test and validate models, but not for their parametrization, nor for the transfer to other sites. Most hydrogeochemical calculations for processes in the NAFB have been carried out using PhreeqC (Parkhurst and Appelo 2013) which was tested for geothermal applications (Hörbrand et al. 2018). Experimental backup was provided by the conversion of the Pullach Th2 well from an injection well to a production well after 5 years of operation. Here, the interactions of the injected cold water with the rock matrix were successfully modeled with an equilibrium model (Baumann et al. 2017). A kinetic PhreeqC model was also used to evaluate the results of the high-temperature aquifer heat storage test (Ueckert and Baumann 2019). Recently, PhreeqC was applied for the thermodynamic modeling of $CaCO_3$ scaling introduced by CO_2 degassing while using inhibitors (Wedenig et al. 2021).

However, PhreeqC falls short for the quantitative prediction of scales in production pipes (Köhl et al. 2020). This is due to the implementation of gas phases in PhreeqC which does not allow a kinetic mass transfer between liquid and gas (Parkhurst and Appelo 2013). Instead, as soon as a gas phase is present, PhreeqC always calculates a full equilibrium between liquid and gas based on Henry's constants and partial pressures.

In order to improve the quantitative predictions of carbonate precipitation, controlled experimental data is required to quantify the stripping process and its effect on pH-value and saturation. With this data, a hybrid model can be developed which calculates the gas–water-exchange in a python script while leaving all other geochemical calculations to PhreeqC. While stripping is the dominant process in geothermal applications, the model should be tested in both directions: precipitation and dissolution of $CaCO_3$.

Controlled laboratory experiments have to be limited to a subset of the complex hydrochemical composition of geothermal fluids, which can contain even considerable amounts of immiscible fluids (Baumann et al. 2017). Inhibition of crystallization has been recorded for ionic strength (Zhang et al. 2019; Qian et al. 2019) and the presence of Magnesium (Berner 1975; Gutjahr et al. 1996; Chen et al. 2006; Sanjuan and Girard 1996). Magnesium not only inhibits the precipitation of calcite but also influences the growth and dissolution of aragonite (Berner 1975; Gutjahr et al. 1996; Chen et al. 2006). Thus, the precipitates built on a surface (e.g., at a wall) and the newly formed particles in solution should be analyzed using microscopic and spectroscopic methods.

This work provides experimental data and a model framework to simulate stripping processes in geothermal systems. Although the experimental conditions do not match

the conditions in geothermal reservoirs exactly, the evaluation with a hydrogeochemical model which has been applied and validated for geothermal systems, allows an extrapolation to geothermal systems.

Materials and methods

Experimental setup of the bubble column

Given the variability of geothermal waters (see, e.g., (Heine et al. 2021)) the experiments were run with Munich tap water (ionic strength: 9.8×10^{-3} mol/L) as a proxy (composition see Table 3). Higher ionic strength (0.0140 and 2.97 mol/L) was established by adding plain table salt (NaCl) to tap water. The water was filled into an acrylic glass column (inner diameter: 0.100 m, height: 1.12 m). Acrylic glass was used to provide visual control on bubble movement and particle formation. Attachment to different pipe materials was not the focus of this study. The gas (air; CO_2, technical grade, Linde, Germany) was evenly injected at 15 cm above the bottom of the column (see Fig. 1) using a 3d-printed air sparging device. The rising gas bubbles ensure a thorough mixing of the solution (Amaral et al. 2018). The gas flow rate was approximately 12 L/h. For the experiments with air the partial pressure of CO_2 was 0.04 bar. For the experiments with CO_2 as gas the partial pressure of CO_2 was slightly above 1.13 bar.

All experiments were performed under ambient conditions (i.e. room temperature and atmospheric pressure). During the experiment, the temperature, the pH value, and the electric conductivity (EC) of the solution were measured continuously with probes (Atlas Scientific, NY, USA) and recorded with an EZO circuit via a Raspberry Pi unit. The recorded water temperature was integrated in the model and can also be seen in Figs. 2, 3, 5, and 7 for selected experiments.

The experiment was started with the injection of air into the solution and terminated when an equilibrium of the pH and EC was reached. Then the water was removed and a sample of the precipitates from the column wall was taken with an adhesive stripe to keep the crystals in its original state. Then the column was filled with a fresh solution and the procedure was repeated until scalings on the column wall were clearly visible.

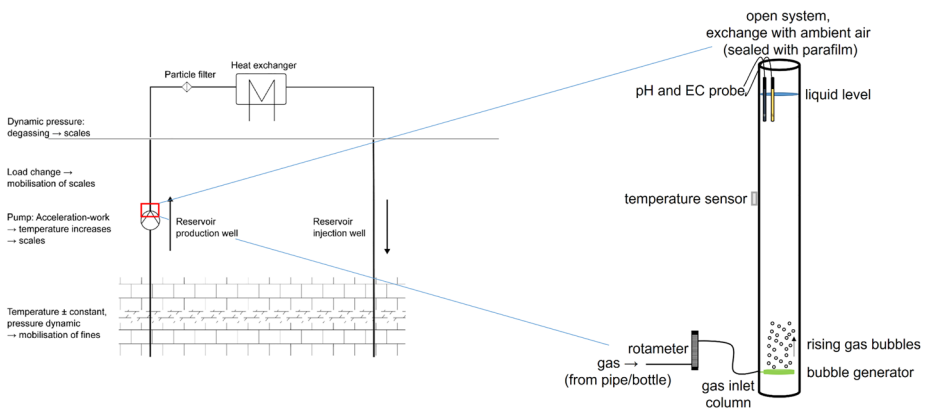

Fig. 1 (left): Schematic figure of geothermal facility highlighting boundary conditions for pressure and temperature which drive the disruption of the lime-carbonic acid-equilibrium, and (right): experimental design to address processes occurring above the submersible pump (highlighted in red) and the disruption of the lime-carbonic acid equilibrium by the presence of a free gas phase

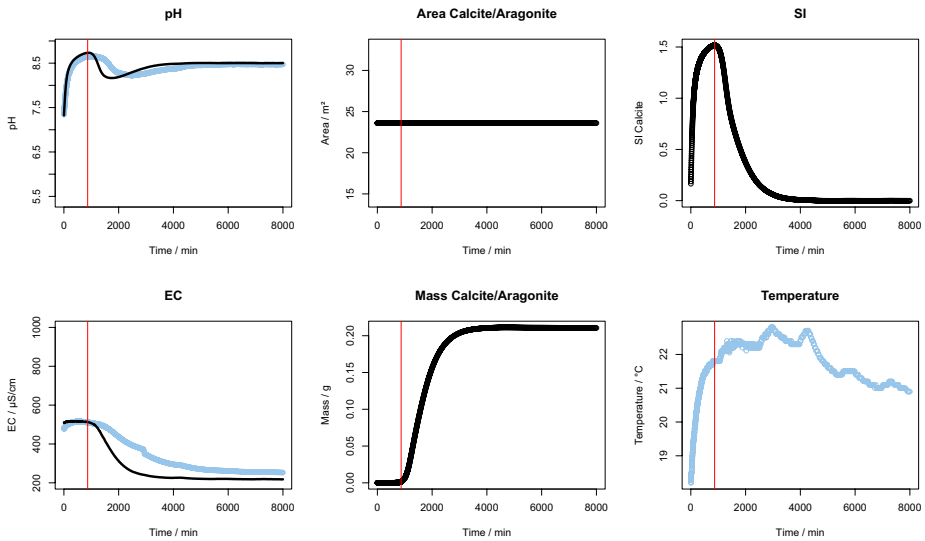

Fig. 2 Parameter development over time for the first run of introducing air into tap water: Comparison of measured (blue) and simulated (black) values; the red line marks the time when the maximum SI is reached and from which precipitation takes place (868 min)

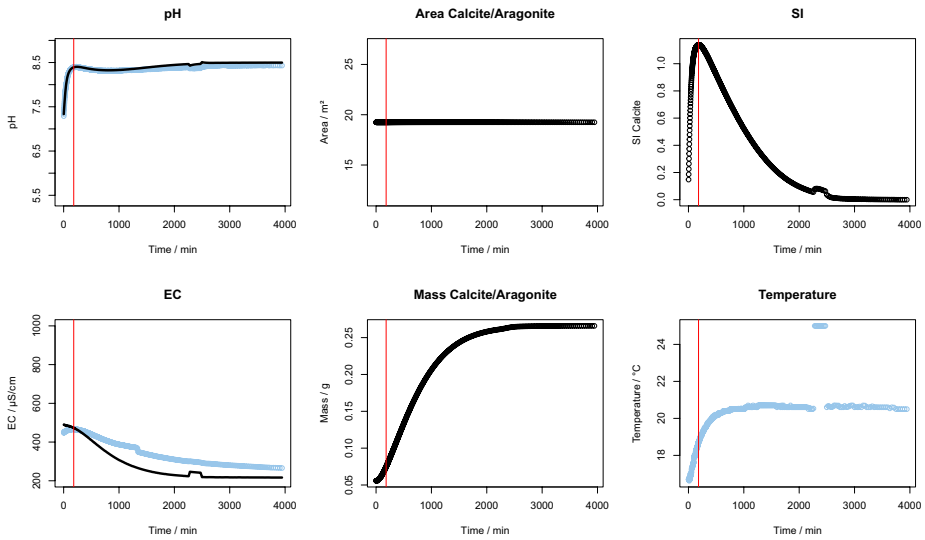

Fig. 3 Example parameter development over time for subsequent runs of introducing air into tap water: Comparison of measured (blue) and simulated (black) values; the red line marks the time when the maximum SI is reached and from which precipitation takes place (182 min)

Afterwards, CO_2 was introduced through the air sparger instead of air to acquire data for the dissolution of the precipitates. Finally, the column wall was acidified with HNO_3 (1.00 M, Carl Roth, Karlsruhe, Germany) to close the mass balance.

Water samples were taken before and after the gas was introduced. During the experiment, no water samples were taken to not disturb the pH sensitive system and in order not to falsify the results of the experiment itself. The concentration of the cations sodium, ammonium, potassium, calcium and magnesium were determined by Ionic chromatography (IC, 881 Compact IC pro, Metrohm Germany; column: C4-150,

Metrohm, Germany). Concentrations of the anions chloride, nitrite, nitrate, phosphate and sulfate were also determined by IC (Dionex IC 1100, ThermoFisher Scientific, USA). The analysis results were validated with an external standard and only used when the deviation was less than 3 %. The alkalinity of tap water was determined by titration. Particles in the solution were collected on polycarbonate filters (0.100 µm, Pieper Filter GmbH).

Samples from the column wall and on the filters were analyzed by Raman spectroscopy (XploRA PLUS, HORIBA, Horiba France SAS).

Hydrogeochemical model

The hydrogeochemical model used PhreeqC (v. 3.6.2), python (v. 3.9.1) and PEST++ (v. 5.0.11). The stock phreeqc.dat thermodynamic database (v. 3.6.2) was used for experiments with tap water and the pitzer.dat database (v. 3.6.2) was used for the experiments with high ionic strength. Reaction rates of $CaCO_3$ were taken from Plummer et al. (1978).

To implement the kinetic mass transfer between gas bubbles and fluid, the model runs were split: A python script prepared the PhreeqC input files and took care of the mass transfer between gas phase and fluid, PhreeqC calculated the actual concentrations, partial pressure, and saturation indices and calculates the kinetics of precipitation and dissolution.

At first, the composition of the fluid (tap water/tap water plus NaCl) was implemented in PhreeqC and the partial pressure for CO_2 in the solution was calculated. At this stage the mass transfer into the bubbles was a fitting parameter which was initialized using the measured bubble dimensions and bubble numbers per liter, the partial pressure of CO_2 in the solution, the partial pressure of CO_2 in the gas phase and the diffusion coefficient across the gas–water-interface. The calculated mass of CO_2 was then introduced as an "effective" gas volume, smaller than the actual volume of the bubble, into the PhreeqC input file for the following simulation where the solution was left to equilibrate kinetically with calcite. After this and any following steps the results were dumped in PhreeqC for the next run. The python code can also handle other gases and could be extended to explicitely calculate the mass transfer across the gas–water-interface, if this data is available.

The fit of the model to the measured data was performed using PEST++. The input files for PEST++ were also prepared with a python script, which is also responsible for collecting the experimental data from the database and plotting the results.

Table 1 shows the initial values of the fitting parameters as well as their range. The initial solutions ion concentrations used in PhreeqC are those of tap water (with added NaCl concentration at higher ionic strength), determined by IC (see also Tables 3 and 4; Additional file 1).

Results and discussion

CO_2 stripping from tap water with air

Figure 2 shows an example for the development of pH, EC, and the saturation index of calcite. Immediately after the air is injected into tap water the pH rises to a maximum but drops again to reach a minimum after roughly 1000 min until it equilibriates at ~ pH

8.45 (see Fig. 2). The development of the pH-value over time was similar for all experiments with air. The times at which the first maximum and the minimum occurred, and thus the dynamics of the pH-change, showed differences that were significant especially between the first and subsequent experiment (see Table 2). The maximum of the pH-values marks the point at which $CaCO_3$ begins to precipitate (Qian et al. 2019) and the concentration of the crystallization seeds is high enough.

When the experiment was performed for the first time, the initial crystallization seeds concentration was close to zero and it took longer until the first seeds were formed. This can be seen in the development of the pH value measured: After starting the injection of air into the with tap water filled column, the pH value increased within 1000 min from 7.34 to a maximum of 8.66. After reaching the maximum, the pH value dropped to 8.22 within the next 1473 min. The minimum showed a wider shape compared to the maximum. From the minimum the pH approached a value of 8.47 which indicates equilibrium conditions.

The numerical model showed that the increase of the pH goes along with an increase of the SI. Again, the first experiment was different and showed higher SI. The maximum of the SI preceded the maximum of the pH. This makes sense because it takes some time to precipitate larger amounts of crystals which would change the pH value.

In this first experiment, the modelled mass of $CaCO_3$ increased from 1.00×10^{-9} g/L (a tiny amount of calcite is required by PhreeqC to simulate kinetic precipitation) to 1.58×10^{-3} g/L in 868 min until the saturation index increased to its maximum of 1.52. The following decrease of the SI indicates precipitation which was also visible at the column walls. The modelled mass of calcite increased continuously to 0.211 g and a plateau was reached. The model results are in agreement with IC measurements of the solution (see Table 3): The difference of the Ca^{2+} concentrations before (= tap water) and after the injection of air was 0.0763 g/L, which corresponds to a $CaCO_3$ concentration of 0.191 g.

The electrical conductivity decreased from 522 μS/cm to 517 μS/cm during the time (868 min) it took to reach the SI maximum; the slight increase in the EC at the beginning can be explained by the temperature dependence of the EC. Only when the precipitation started, the EC also decreased continuously—following the decrease of the Ca^{2+} concentrations in the solution—and reached a plateau at $\sim$ 245 μS/cm. The modeled EC value at the end was 218 μS/cm. The discrepancy here can be explained mainly by the fact that the used sensor did not detect the range between 380 and 330 μS/cm correctly and therefore provided an incorrect final value.

The development of pH and SI over time can be interpreted as follows: the injection of air strips CO_2 from the solution and shifts the pH to higher values (Eqs. 1–3). Consequently, the SI for $CaCO_3$ increases. Precipitation of $CaCO_3$ does not start immediately but only after first nuclei have formed. This explains the difference between first and subsequent runs.

In the subsequent experiment with tap water (Fig. 3), the pH value increased from 7.29 to a maximum of 8.41 within 232 min. The pH value then decreased to a minimum of 8.31 within the next 545 min and approached a value of 8.43 from that, again indicating equilibrium conditions. The model for the second experiment started with an initial mass of calcite of 5.57×10^{-2} g/L (representing that precipitates have already built on

the column wall) and increased to 7.48×10^{-2} g/L in the 182 min it took to reach the SI maximum of 1.14. The SI then dropped and the mass increased continuously until a plateau was reached at 2.66×10^{-1} g/L (the Δ (end–start) is equal to the modeled mass of $CaCO_3$ at the end of the first experiment). The IC measurement confirmed this: The difference between the Ca^{2+} concentrations before and after the experiment was 0.0728 g/L corresponding to a $CaCO_3$ concentration of 0.182 g/L. This is again in very good agreement to the modeled mass of precipitated $CaCO_3$ during this experiment.

The EC decreased from 509 μS/cm to 505 µS/cm in the time it took to reach the SI maximum. After precipitation took place, the EC decreased continuously until a plateau was reached at ~ 265 µS/cm; the calculated EC at the end was 217 µS/cm. The reason for this discrepancy is, as mentioned above, the sensor used.

Regarding the IC measurements (see Table 3), the amount of precipitates formed did not vary between the first and the subsequent experiments. However, the time it took to reach the maximum SI as well as the first pH maximum—marking the beginning of precipitation—differed between the experiments by 686 min (SI) and 768 min (pH). This can be explained by the formation of crystallization seeds which takes longer in a freshly cleaned column than in a column where crystals are already on the column wall. As can be seen in Table 2 there was no significant difference between measured and modeled values.

Most of the crystals at the bottom presumably have been removed with the change of the water of the column and could not be quantified in most selected runs. Before the acidification of the column (wall), 1.65 g solid $CaCO_3$ have been collected from the column bottom. On the polycarbonate filters from the water samples taken after selected runs (filtered volume ca. 0.50 L, 0.100 µm) no crystals have been found.

The particles taken from the column wall were needle shaped and were identified as aragonite by Raman spectroscopy (see Fig. 4). The length and width of the particles was 19.5 ± 7.46 μm and 4.35 ± 1.76 μm, respectively.

Assuming cylindrical particles and taking the total mass of Ca^{2+} on the column wall of 3.58 g Ca^{2+} (= 8.94 g $CaCO_3$) after final acidification of the column, the calculated surface area of $CaCO_3$ was 32.6 ± 8.89 m^2/mol (10 microscopic images were selected for this calculation). The high standard deviations of the particle sizes and the destructive sampling of particles from the column walls did not allow to assess the growth of the

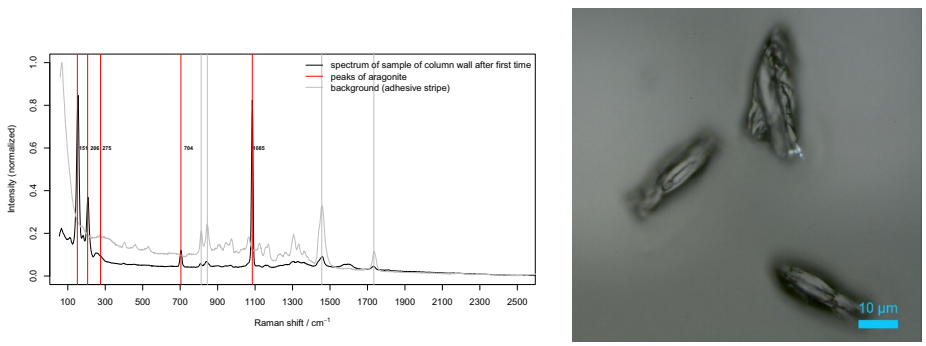

Fig. 4 (left): Raman spectrum (averaged), and (right): corresponding microscopic image (100x LWD objective) of the particles from the column wall after the injection of air into tap water; red lines show the peaks of aragonite (Gabrielli et al. 2003, grey lines show the peaks of the background (adhesive stripe)

particles experimentally. However, the calculated specific surface area served as an initial value (3.00×10^5 cm^2/mol) in the PEST++ fitting procedure.

The mass balance obtained after acid treatment of the column showed that after nine experiments using air to strip CO_2, a total of 78.6% of the available Ca^{2+} precipitated, which means that full stripping occurred. 59.8 % of the $CaCO_3$ precipitates were attached to the column wall, the rest precipitated as particles in the solution which was exchanged at the end of each experiment.

Influence of ionic strength on CO_2 stripping and $CaCO_3$ precipitation

To cover a broader range of potential geothermal waters, experiments were repeated at higher ionic strength. A slightly elevated ionic strength of 1.40×10^{-2} mol/L showed a similar behavior in the development of the measured pH and EC during the first and subsequent injections of air, as well as in the calculated values of pH, EC and SI, mass and area of $CaCO_3$ (see Fig. 5) as in the experiments with tap water ($I = 9.83 \times 10^{-3}$ mol/L).

In comparison to the experiments with plain tap water, it took longer to reach the pH maximum: 530 min longer for the first run where air was introduced into the solution with $I = 1.40 \times 10^{-2}$ mol/L and 131 min for one selected subsequent experiment (for absolute values see Table 2; the selected experiment is a representative for the subsequent experiments). The difference between the first runs of the experiments performed can also be explained by the fact that the sensor did not work for 300 min during the experiment with higher ionic strength and the next recorded value was at a slightly higher temperature. The modeled value for the time difference between the first runs of the experiments until the pH maximum was reached was 129 min. This trend, that it generally took longer to reach the pH maxima at a slightly higher ionic strength than plain tap water also applied to the other calculated values (e.g. SI maximum of 1.67 after 964 min at $I = 1.40 \times 10^{-2}$ mol/L; plain tap water: SI maximum of 1.52 after 868 min).

Another difference between the experiments with plain tap water and slightly higher ionic strength is shown by the samples taken from the column wall after selected experiments. At higher ionic strength they showed cubic crystals with a length of 23.8 ± 0.257 μm and a width of 19.2 ± 1.47 μm. The crystals could be identified as calcite by Raman spectroscopy (see Fig. 6)—in contrast, aragonite was identified in the experiments with plain tap water.

This is in line with previous work, which showed that salinity influences the polymorphic form of the precipitates. The precipitation rate of aragonite decreases with an increasing salinity (Zhong and Mucci 1989; Morse et al. 2007) and increasing NaCl concentrations accelerate the transformation of aragonite to calcite (Bischoff and Fyfe 1968). Reports that calcite was the predominant polymorph at higher salinity (Zhang et al. 2019) are consistent with this work.

The ionic strength of $I = 1.40 \times 10^{-2}$ mol/L was obviously too weak for proper inhibition, additionally the fact comes into play that at higher ionic strength the solubility of gases decreases, which means that the effect of stripping is emphasized. This might indicate that the rather fast stripping of CO_2 leads to local precipitation around the bubbles. However, the reaction rates without crystallization nuclei at the walls were generally slower, as indicated by the times to reach the pH maximum (1030 min without crystallization nuclei vs. 262 min with crystallization nuclei present; for

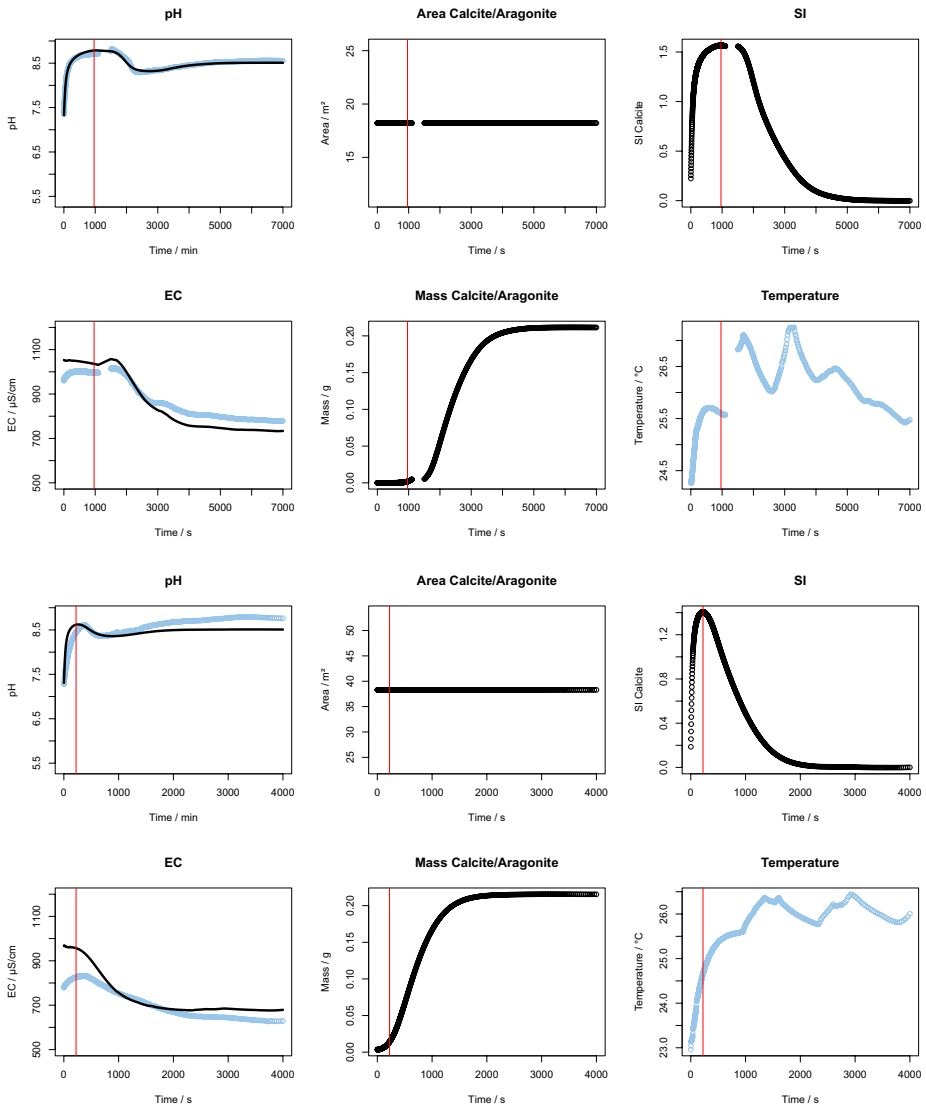

Fig. 5 (top): Parameter development over time for the first and (bottom): selected subsequent run of introducing air into water with an ionic strength of 1.40×10^{-2} mol/L: Comparison of measured (blue) and simulated (black) values; the red line marks the time when the maximum SI is reached (a: 964 min, b: 223 min)

clarification and to avoid the error of the sensor, modeled values of the experiments with higher ionic strength are mentioned here).

The mass balance after acid treatment of the column showed that 76.7% of the Ca^{2+} precipitated as $CaCO_3$, which means a full stripping occurred, equally to the mass balance of the experiment with plain tap water. But, in contrast to the experiment conducted with plain tap water, no particles could be collected from the bottom of the column and 81.5% of the $CaCO_3$ precipitates were attached to the column wall. The summary of ionic concentrations determined by IC of the experiments of injecting air into water with an ionic strength of $I = 1.40 \times 10^{-2}$ mol/L can be found in Additional file 1.

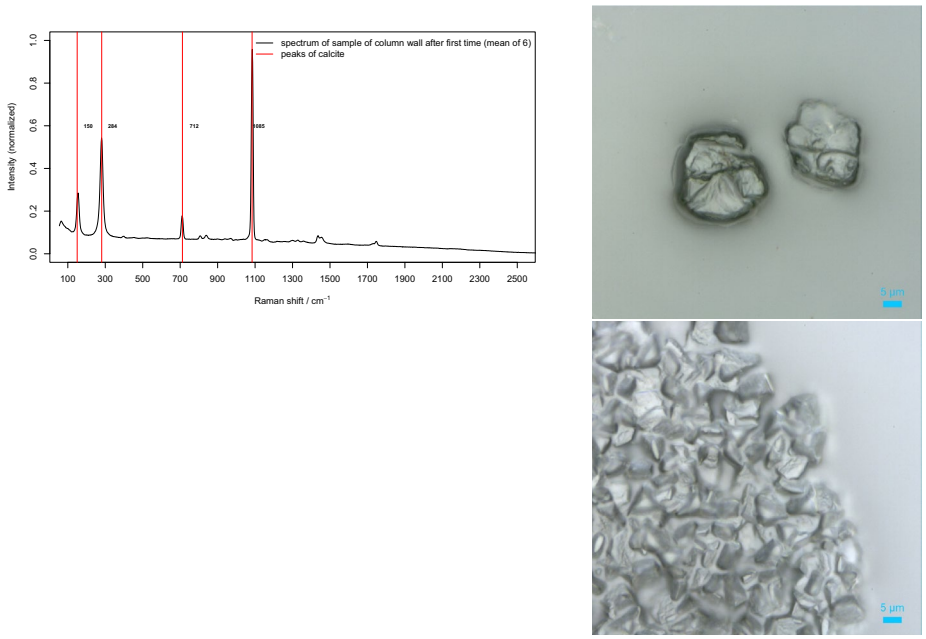

Fig. 6 (left): Raman spectrum (averaged) and (right): corresponding microscopic images of the particles from the column wall after injecting air into the aqueous solution of high ionic strength (1.40×10^{-2} mol/L); red lines show the peaks of calcite (Gabrielli et al. 2003; Dandeu et al. 2006)

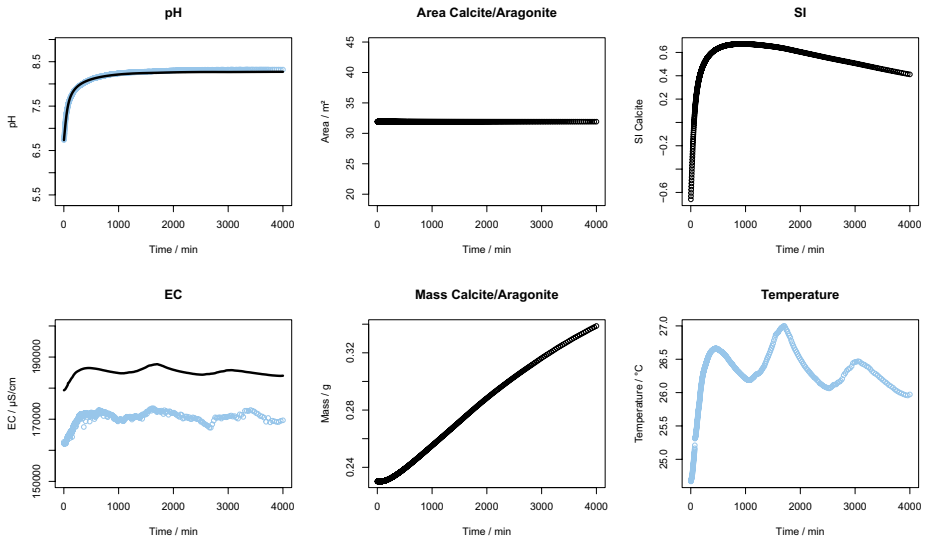

Fig. 7 Parameter development over time during the injection of air into water with an ionic strength of 2.97 mol/L: Comparison of measured (blue) and simulated (black) values

The injection of air into water with a higher salinity content (tap water with ~ 120 g/L NaCl, I = 2.97 mol/L) resulted in the well known sharp increase of the pH value at the start of the experiment. However, instead of decreasing then, it continuously increased to a pH value of ~ 8.32 (see Fig. 7). This indicates that no precipitation occurred.

The samples taken from the column wall showed cubical shaped crystals. No $CaCO_3$ specific Raman spectra (see Fig. 8) were detected and the crystals were NaCl which is

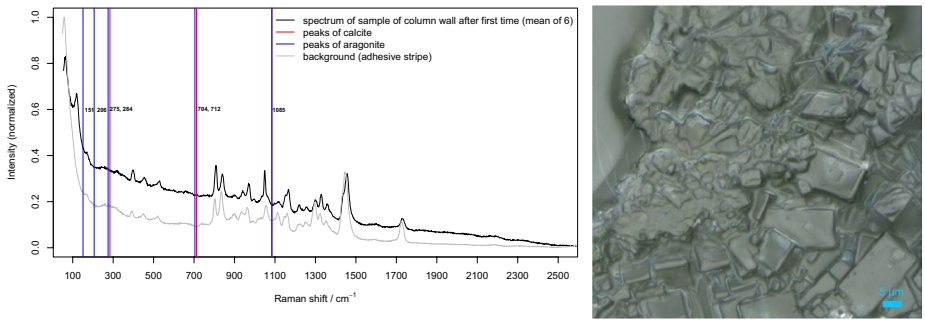

Fig. 8 (left): Raman spectrum of the particles from the column wall after injecting air into the aqueous solution of high ionic strength (2.97 mol/L) and (right): the corresponding microscopic image; red lines show the peaks of calcite and blue lines of aragonite (Gabrielli et al. 2003; Dandeu et al. 2006)

commonly formed after drying. This also demonstrates that the precipitation of $CaCO_3$ was inhibited at the ionic strength of 2.97 mol/L. Due to the high NaCl content, the concentrations of Ca^{2+} and Mg^{2+} were below the limit of detection of the IC, so that a direct validation by a mass balance was not achievable.

For the simulation of this series of experiments, the thermodynamic database pitzer.dat was used to reflect the high salinity. The model results showed a slight increase of the mass of $CaCO_3$ from 0.230 to 0.339 g/L which means that 0.109 g/L $CaCO_3$ should have precipitated. In accordance to the increase of the mass in the model, the SI also increased from −0.660 to a maximum of 0.673 after 930 min and then slightly decreased to 0.412, also indicating that a precipitation should take place. This is in contrast to the samples taken from the column wall, where no $CaCO_3$ could be detected. It is also in contrast to previous work: It was shown that high salinity prolonged the $CaCO_3$ crystallization (Qian et al. 2019) and that high salinity content hindered the $CaCO_3$ precipitation (Zhang et al. 2019). This supports our experimental findings and reflects a low sensitivity of the model. When the area of $CaCO_3$ was set to zero and was not adjusted by PEST++, the mass did not change either and was calculated by the model to a value of 1.00×10^{-7} g. The SI increased to 0.958 but showed no sign of precipitation occurring, i.e. no decrease. The parameter development without fitting the area is shown in Additional file 1.

The salinity of the solution in this set of experiments was clearly outside the precision range for the EC probe. This explains the offset between measured values and model data. Still, the lines are roughly parallel, indicating that all significant processes in the column are covered in the model.

Dissolution of carbonate scales through CO_2-sparging

The use of CO_2 in geothermal applications is considered a minimal invasive, environmentally friendly method to prevent and remove scalings. To test the kinetics of scale removal by CO_2, scales at the column wall were prepared in another experiment. Then pure CO_2 was injected as gas phase, which is equivalent to the injection of CO_2 below the submersible pump in geothermal applications.

Figure 9 shows the development of the measured and simulated parameters after CO_2 -injection. The pH decreased from 8.30 to a minimum of 5.55 and then slowly increased to an end value of 6.19. It took just 40 min to reach the pH minimum, indicating that

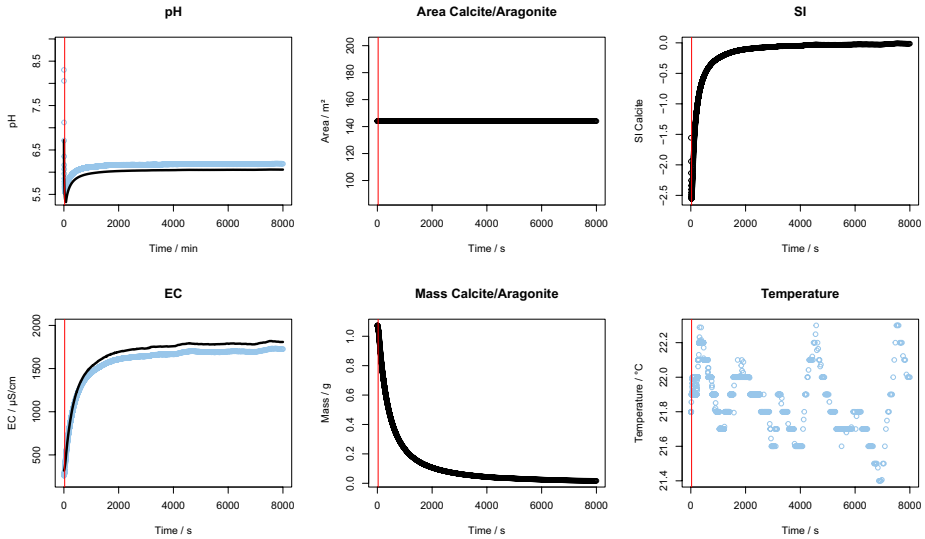

Fig. 9 Parameter development over time when introducing CO_2 into water: Comparison of measured (blue) and simulated (black) values; the red line marks the time (28 min) when the minimum SI is reached

the dissolution of $CaCO_3$ begins much earlier than the precipitation. This makes sense because the dissolving of $CaCO_3$ can start when the equilibrium is disrupted but for precipitation crystallization seeds have to be present first. The model showed that the minimum SI of −2.56 is reached after 28 min and then increased continuously to an end value of −0.014. The negative SI and the development of the pH value prove a net mass transfer of CO_2 from the CO_2 bubbles into the water and thus a disruption of the lime-carbonic acid equilibrium and the dissolution of solid $CaCO_3$ from the column wall. The calculated mass of $CaCO_3$ decreased from 1.07 to 1.06 g/L in the first 28 min and continuously decreased to 0.0170 g/L at the end. This was validated by the IC measurements (see Table 4): The difference of the Ca^{2+} concentration before and after the first injection of CO_2 was 0.431 g/L, which corresponds to a $CaCO_3$ concentration of 1.08 g/L. This differs by 0.0190 g/L ($\widehat{=}$ 1.80%) from the calculated dissolved $CaCO_3$ mass. The first and subsequent run of this experiment hardly differed (the parameter development of a subsequent run is shown in Additional file 1). A comparison of pH minima is shown in Table 2. Again, there is no significant deviation between measured and modeled values.

The very quick dissolution of $CaCO_3$ scalings from the column wall after introducing CO_2 into the solution is also shown in the behavior of the EC: It increased continuously from 248 µS/cm until an end value of 1813 µS/cm was reached. The calculated EC was 1808 µS/cm which means a deviation of 5.00 µS/cm ($\widehat{=}$ 0.276%) from the measured value, far less than in the experiment with air, which indicates that the deviation of the final EC value between measurements and model results at lower EC is likely a bug in the firmware of the used system.

In contrast to the precipitation experiments, the samples taken from the column wall after the first injection of CO_2 into the water filled column showed not only needle-shaped particles which were identified as aragonite, but also particles identified as calcite by Raman spectroscopy (see Fig. 10). This transformation of aragonite into calcite is accelerated by high CO_2 pressures (Bischoff and Fyfe 1968; Fyfe et al. 1965).

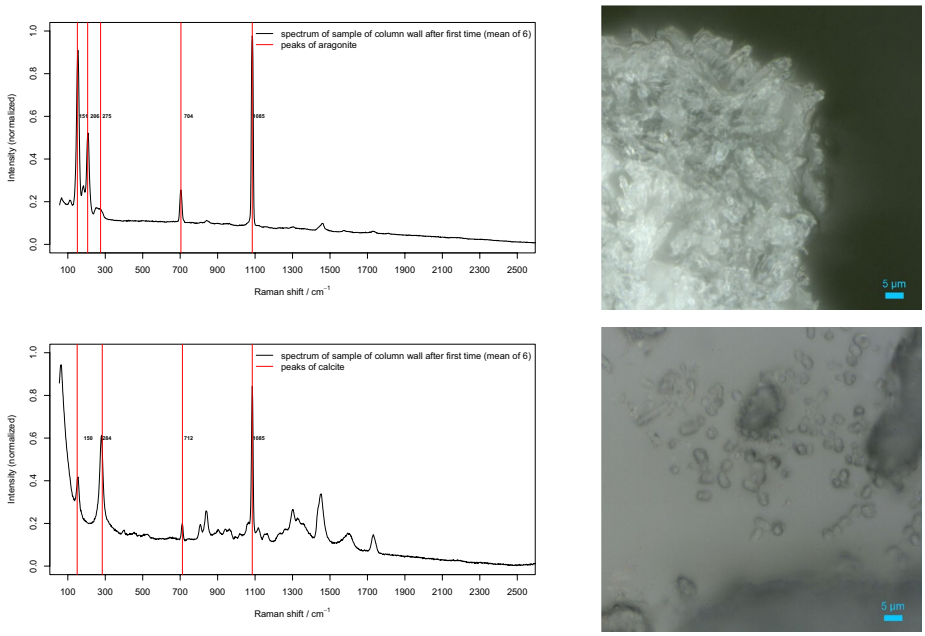

Fig. 10 (left): Raman spectra of the particles from the column wall after injecting CO_2 into the aqueous solution and (right): the corresponding microscopic images (100x LWD objective); red lines show the peaks of aragonite and calcite (Gabrielli et al. 2003; Dandeu et al. 2006)

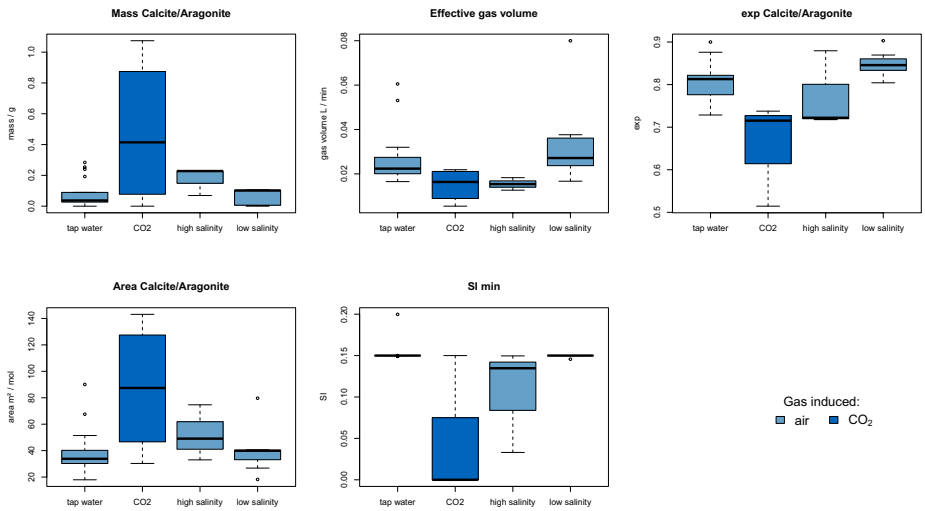

Fig. 11 Box plots of mass, area and exp of $CaCO_3$, the SI min and the effective gas volume for the simulations of the experiments of introducing air into tap water and water with high ionic strength (1.40×10^{-2} mol/L and 2.97 mol/L) and introducing CO_2 into tap water

Parameter analysis

The model results for the different experiments are compared in Fig. 11: It shows the boxplots of the parameters initial mass, area and exponent of $CaCO_3$ as well as the SI when mineralisation takes place (SI min) and the effective gas volume for the simulations of the experiments conducted.

Table 1 Parameters adjusted by PEST++, initial value and range

	Unit	Initial value	Range	
Mass $CaCO_3$	mol	1.00×10^{-9}	1.00×10^{-10}	-1.00×10^{-1}
Area $CaCO_3$	cm^2/mol	3.00×10^{5}	1.00×10^{4}	-1.00×10^{8}
Gas volume	L per timestep	3.20×10^{-2}	5.00×10^{-6}	-8.00×10^{-2}
SI mineralisation	–	0.150	0	− 0.400
Exponent $CaCO_3$ (M/M_0)	–	0.900	0.500	− 1.00

Table 2 Maxima and minima of pH value in the conducted experiments, comparison of measured and modeled values

	pH maximum	Within time, / min	pH minimum	Within time, / min
CO_2 stripping from air				
Tap water				
First run—measured	8.66	1000	8.22	2470
First run—modeled	8.73	901	8.16	1760
Subsequent run—measured	8.41	233	8.31	778
Subsequent run—modeled	8.40	242	8.32	802
$I = 1.40 \times 10^{-2} mol/L$				
First run—measured	8.83	1530	8.29	2410
First run—modeled	8.79	1030	8.32	2720
Subsequent run—measured	8.61	364	8.36	697
Subsequent run—modeled	8.62	262	8.36	886
Dissolution of $CaCO_3$ with CO_2				
Tap water				
First run—measured	–	–	5.55	40.0
First run—modeled	–	–	5.53	74.0
Subsequent run—measured	–	–	5.65	64.0
Subsequent run—modeled	–	–	5.58	50.0

Table 3 Concentration of the ions of the solutions in mg/L (± standard deviation) before and after the injection of air into tap water and the mass balance after acidification of the column wall (in mg)

	Before (tap water)		After		∑ end	∑ start	Δ (start–end)	Acidification	
	mg/L		mg/L		mg	mg	mg	mg	
Na^+	4.088	0.866	4.22	0.381	364	331	– 32.8	28.8	8.69
NH_4^+	n.d.		n.d.		n.d.	n.d.	n.d.	n.d.	
K^+	1.20	0.101	1.46	0.0898	122	97.4	– 24.8	n.d.	
Ca^{2+}	93.9	8.31	28.2	1.95	1628	7610	5982	3578	96.9
Mg^{2+}	23.6	1.36	19.7	1.42	1878	1909	30.9	n.d.	
Cl^-	12.7	0.0585	13.7	0.0800	1151	1032	– 119	149	0.276
NO_2^-	n.d.		n.d.		n.d.	n.d.	n.d.	17.8	0.833
NO_3^-	8.98	0.125	6.65	0.01732	641	727	85.8	22927	43.8
PO_4^{3-}	n.d.		n.d.		n.d.	n.d.	n.d.	n.d.	
SO_4^{2-}	6.68	0.0279	12.8	0.0306	755	541	– 214	45.0	0.102

Table 4 Concentration of the ions in mg/L (± standard deviation)—descaling with CO_2, before and after injecting the gas until an equilibrium was reached, as well as the mass balance of all CO_2 cycles and the scaled column (mg)

	Before		After		∑ CO_2 cycles	Δ $CO_{2\,start}$ - $CO_{2\,end}$	∑ precipitated
	mg/L		mg/L		mg	mg	mg
Na^+	4.088	0.866	n.d.		9.53	6.58	− 82.5
NH_4^+	n.d.		n.d.		n.d.	n.d.	n.d.
K^+	1.20	0.101	4.03	0.483	9.82	4.68	− 45.0
Ca^{2+}	93.9	8.31	452	0.904	1101	798	7922
Mg^{2+}	23.6	1.36	27.0	0.433	103	7.90	− 108
Cl^-	12.7	0.0585	8.19	0.257	299	172	− 72.5
NO_2^-	n.d.		n.d.		n.d.	n.d.	n.d.
NO_3^-	8.98	0.125	2.71	0.0252	103	213	31.7
PO_4^{3-}	n.d.		n.d.		n.d.	n.d.	n.d.
SO_4^{2-}	6.68	0.0279	3.20	0.04000	92.7	151	− 73.8

The initial mass, the area and the exponent of $CaCO_3$ are important for the overall reaction rate (R, in mol/L·s) of the precipitation of $CaCO_3$ (Appelo and Postma 2005):

$$R = r \cdot \frac{A_0}{V} \cdot (\frac{m_t}{m_0})^n \cdot g(C) \tag{5}$$

with r the specific reaction rate (mol/m^2 ·s), the $CaCO_3$ surface area A_0 (m^2), the volume V (m^3), the initial moles (m_0) and the moles at specific time (m_t) of $CaCO_3$. n provides information about the change of surface/volume during dissolution and *g(C)* includes effects of the solution on the rate (Appelo and Postma 2005).

The exponent of $CaCO_3$ (exp) comes into effect when the initial mass is greater than 0, then the area A in the simulation is defined as:

$$A = SSA \cdot M_0 \cdot (M/M_0)^{\exp} \tag{6}$$

with SSA the specific surface area (cm^2/mol), M_0 the initial mass (mol), and M the current mass (mol) of $CaCO_3$.

For the parameter discussion, the data situation has to be considered: The experiments of tap water and water of low ionic strength ($I = 1.40 \times 10^{-2}$ mol/L) with air were carried out more often (providing 18 and 7 data points respectively from the parameter adjustment) than the experiments of tap water with CO_2 and water of high ionic strength (I = 2.97 mol/L) with air (with only 4 and 3 data points respectively).

Affected are the mass, the surface area, and the parameter which controls the surface-to-mass ratio in the kinetic equations (exp Calcite/Aragonite). Except for the experiments with CO_2-injection the variation between experiments was rather small. The values for the initial mass in the CO_2 experiment was the highest and the lowest in comparison to the other experiments (first run of the CO_2 experiment: 1.07 g; last run of the CO_2 experiment: 1.00×10^{-8} g). This makes sense, because during the experiments with CO_2 the carbonates were removed from the column wall. In all other experiments the carbonates at the column wall seem to react with an effective mass (consider a multilayer scaling where only the topmost precipitates react): The initial mass differed only

by 0.0184 g between the parameter adjustments for the experiments with tap water (mc: 0.0793 g) and water with an ionic strength of 1.40×10^{-2} mol/L (mc: 0.0609 g), which can also be explained by the nature of these experiments: They only differed in the ionic strength of the solution and the formed polymorph of $CaCO_3$, but not the amount of precipitates built (as discussed above). The average initial mass of the experiment of the solution of high ionic strength ($I = 2.97$ mol/L) with air was 0.176 ± 0.0924 g which is contrary to the fact that no precipitates formed and the column was cleaned before the start of the experiment. The reason here is likely the simulation itself and the insensitivity of the initial mass of $CaCO_3$ as mentioned above.

The results of the high salinity experiments also stand out with higher surface areas. Here the surface-to-mass exponent was lower compared to the other experiments of CO_2 stripping from air (I = 2.97 mol/L, exp: 0.773 ± 0.0922; I = 1.40×10^{-2} mol/L, exp: 0.849 ± 0.0312; tap water, exp: 0.807 ± 0.0407). This indicates that the inhibition of scalings at high ionic strength in the experiment was lower compared to the theoretical inhibition. In the model this was compensated by higher masses and surface areas.

The effective gas volume, i. e., the mass transfer between gas bubbles and solution, was slightly lower for the experiments with CO_2-injection (0.0150 ± 0.00761 L) and high salinity (0.0155 ± 0.00282 L). For high ionic strength this can be explained with the lower solubility (= higher partial pressures) of the gases. Here, less air is needed to strip the CO_2. For CO_2-injection, the lower effective gas volume can be explained with the high partial pressure of CO_2 in the gas phase, which results in a higher gradient for dissolved CO_2 around the bubbles and increased diffusive mass transfer in the solution. *Vice versa* this also explains the higher effective gas volume for the experiments of tap water with air (0.0262 ± 0.0119 L) and water with an ionic strength of 1.40×10^{-2} mol/L with air (0.0348 ± 0.0212 L) (low partial pressure of CO_2 in gas phase, gradient, mass transfer in gas bubble).

The model introduced a minimum SI value for initial precipitation and all precipitation experiments showed roughly the same positive value. This reflects an initial oversaturation before precipitation can start. For the experiment with tap water (0.153 ± 0.0118) and water with low ionic strength (0.149 ± 0.00166), the SI min hardly deviated from the start value of SI min (0.150) in the PEST++ adjustment. The adjustment of SI was tested in a range between 0.0500 and 0.400 for the experiment of tap water with air and it resulted that the simulation was insensitive to the actual value of the minimum saturation index as long as it was positive. This makes sense because the SI rose quickly immediately after the stripping started. Therefore, a higher minimum SI, which reflects the delay due to the formation of initial crystallization nuclei, shifts the beginning of crystallization only very slightly. As geothermal waters are never free of particles, the presence of crystallization nuclei is not a limiting factor. Here, the model could drop this extra boundary condition. The SI min of the CO_2 experiment had the highest deviation which is caused by the high starting pH in the first experiment providing a SI min of 0.15. In the remaining CO_2 experiments the SI min was 0.00 since no precipitation and only dissolution of $CaCO_3$ occurred, it makes sense that here no oversaturation is required. The SI min of the experiment with the high ionic strength (I= 2.97 mol/L) was 0.106 ± 0.0634. $CaCO_3$ growth initiates with the formation of surface nuclei when the saturation state is greater than 2 ($\widehat{=}$ SI of 0.301) (Dove and Hochella 1993).

The area of $CaCO_3$ was the highest in the experiment of tap water with CO_2 (87.1 ± 50.2 m^2/mol) which can be explained by—same as in the case of the mass of $CaCO_3$—the experiment: At the start, scaling of $CaCO_3$ was attached on the column wall resulting in a high area (143 m^2/mol) but by dissolving it with CO_2, the area decreased (30.3 m^2/mol). For the experiment of high ionic strength (I = 2.97 mol/L) with air the simulated value for the area of $CaCO_3$ was 52.2 ± 21.0 m^2/mol which is high considering the fact that no $CaCO_3$ precipitates. This could be counteracted by setting the area to zero and not adjusting it in this particular case. The values of the area of $CaCO_3$ differed only by 2.37 m^2/mol between the experiments of tap water (38.3 ± 16.7 m^2/mol) and water with ionic strength of I = 1.40×10^{-2} mol/L (40.7 ± 19.2 m^2/mol) with air and are in range with the calculated value from the microscopic images (30.0 m^2/mol).

Conclusion

With our work we could validate the effect of stripping on carbonate precipitation and the disruption of the lime–carbonic-acid equilibrium by experiments and a hydrogeochemical model. As scalings in geothermal systems are strongly connected to the formation of gas bubbles, the experimental set up was a column filled with a solution where gas was introduced at the bottom. To cover a broader range of geothermal waters, the ionic strength of the solution was varied at the experiments of introducing air: At I = 9.80×10^{-3} mol/L (tap water) 59.8% of the precipitated $CaCO_3$ remained attached to the column wall, at I = 1.40×10^{-2} mol/L 81.5% and at I = 2.97 mol/L the precipitation was inhibited. By introducing CO_2 into a scaled column filled with tap water, the scaling from the column wall dissolved completely. The ionic strength had also an influence on the built polymorph: When tap water was used, aragonite was formed and at I = 1.40×10^{-2} mol/L calcite was formed. Introducing of CO_2 resulted in a change of the polymorphic form from aragonite to calcite, both polymorphs were present.

Precipitation took longer in experiments where air was introduced into a clean column compared to a column with some scalings present. This can be explained by the presence of crystallization nuclei. There was, however, no difference in the amount of scalings at the column wall. It should also be noted that geothermal waters always contain crystal particles and therefore this difference should not be observed in natural systems.

The precipitation of $CaCO_3$ by stripping of CO_2 from the solution into the gas phase cannot be simulated using stock PhreeqC model, because the gas phases in PhreeqC always equilibrate fully and instantaneous. The kinetic exchange between gas phase and water phase was implemented externally using a python script. With this, the model calculates the pH and EC as well as the precipitated mass correctly. Inhibition and dissolution of carbonate precipitation could also be covered in the model.

The parameter adjustment of the hydrogeochemical model with PEST++ showed that the input parameters (SI min, effective gas volume, exp $CaCO_3$, mass $CaCO_3$ and area $CaCO_3$) variation was rather small for the precipitation experiments. The adjustment also revealed that the minimum saturation index, which translates into the time it takes to form initial crystallization nuclei, is an insensitive parameter. For the dissolution of

$CaCO_3$ with CO_2 the variation of the input parameters was high because of the nature of the experiment (e.g., really high area of $CaCO_3$ at the start (143 m^2/mol) vs. small area of $CaCO_3$ at the end (30.3 m^2/mol)).

While this work lays the foundation for a process based prediction of the scales in geothermal systems, future work has to address dynamic conditions (e.g., shear stress) and different materials.

Abbreviations

EC	Electrical conductivity
exp	Exponent of $CaCO_3$, controls surface to mass ratio
I	Ionic strength
IC	Ionic chromatography
ID	Inner diameter
IAP	Ion activity product
K_{sp}	Solubility product
mc	Initial mass of $CaCO_3$
NAFB	North Alpine Foreland Basin
$p(CO_2)$	Partial pressure of CO_2
SSA	Specific surface area
SI	Saturation index

Supplementary Information

The online version contains supplementary material available at https://doi.org/10.1186/s40517-023-00256-4.

Additional file 1: **Figure S1**. Parameter analysis: Box plots of the SI min value for the simulationsof the experiments of inducing air into tap water, when the input values arechanged. Figure S2. Parameter analysis via PEST++: Box plots of the gas volume valuefor the simulations of the experiments of inducing air into tap water, when theinput values are changed. Figure S3. Parameter analysis via PEST++: Box plots of the CaCO3 area valuefor the simulations of the experiments of inducing air into tap water, when theinput values are changed. Figure S4. Parameter analysis via PEST++: Box plots of value of the mass ofCaCO3 for the simulations of the experiments of inducing air into tap water,when the input values are changed. Figure S5. Parameter analysis via PEST++: Box plots of exp CaCO3 for thesimulations of the experiments of inducing air into tap water, when the inputvalues are changed.

Acknowledgements
Financial support by BMWK/ZIM and the Geothermal-Alliance Bavaria is gratefully acknowledged. We thank Jaroslava Obel for the measurements of the anions by IC.

Author contributions
LZ organized and performed the experiments, did the scaling analysis and evaluated the experimental data. TB initiated the project, had the idea and developed the hydrogeochemical modeling framework. LZ and TB discussed the results which emerged in a refinement of the model. All authors read and approved the final manuscript.

Funding
This project was partially funded by the Federal Ministry for Economic Affairs and Climate Action (BMWK) in the framework of ZIM, "Central Innovation Programme for small and medium-sized enterprises (SMEs)", and the Bavarian Ministry of Science and Art within the project Geothermal-Alliance Bavaria.

Availability of data and materials
The data sets generated and analyzed during the current study are available from the corresponding author on reasonable request.

Declarations

Competing interests
The authors declare that they have no competing interests.

Received: 20 September 2022 Accepted: 13 April 2023
Published online: 30 April 2023

References

Amaral A, Bellandi G, Rehman U, Neves R, Amerlinck Y, Nopens I. Towards improved accuracy in modeling aeration efficiency through understanding bubble size distribution dynamics. Water Res. 2018;131:346–55. https://doi.org/10.1016/j.watres.2017.10.062.

Appelo CAJ, Postma D. Geochemistry, Groundwater and Pollution. 2nd ed. Amsterdam: AABalkema Publishers; 2005. https://doi.org/10.1201/9781439833544.

Baumann T, Bartels J, Lafogler M, Wenderoth F. Assessment of heat mining and hydrogeochemical reactions with data from a former geothermal injection well in the malm aquifer, bavarian molasse basin, germany. Geothermics. 2017;66:50–60. https://doi.org/10.1016/j.geothermics.2016.11.008.

Berner RA. The role of magnesium in the crystal growth of calcite and aragonite from sea water. Geochimica et Cosmochimica Acta. 1975;39(4):489–504. https://doi.org/10.1016/0016-7037(75)90102-7.

Bischoff JL, Fyfe WS. Catalysis, Inhibition, and the Calcite-Aragonite Problem. I. The Aragonite-Calcite Transformation. Am J Sci. 1968;266:65–79.

Chang R, Kim S, Lee S, Choi S, Kim M, Park Y. Calcium carbonate precipitation for co2 storage and utilization: A review of the carbonate crystallization and polymorphism. Front Energy Res. 2017;5:682.

Chen T, Neville A, Yuan M. Influence of Mg^{2+} on $CaCO_3$ formation–bulk precipitation and surface deposition. Chem Eng Sci. 2006;61(16):5318–27. https://doi.org/10.1016/j.ces.2006.04.007.

Dandeu A, Humbert B, Carteret C, Muhr H, Plasari E, Bossoutrot JM. Raman Spectroscopy - A Powerful Tool for the Quantitative Determination of the Composition of Polymorph Mixtures: Application to $CaCO_3$ Polymorph Mixtures. Chem Eng Technol. 2006;29(2):221–5. https://doi.org/10.1002/ceat.200500354.

Dove PM, Hochella MF. Calcite precipitation mechanisms and inhibition by orthophosphate: In situ observations by scanning force microscopy. Geochimica et Cosmochimica Acta. 1993;57(3):705–14.

Eyerer S, Schifflechner C, Hofbauer S, Wieland C, Zosseder K, Bauer W, Baumann T, Heberle F, Hackl C, Irl M, Spliethoff H. Potential der hydrothermalen geothermie zur stromerzeugung in deutschland; 2017.

Fyfe WS, Bischoff JL, Pray LC, Murray RC. The Calcite-Aragonite Problem. In: Dolomitization and Limestone Diagenesis, vol. 13. Germany: SEPM Society for Sedimentary Geology; 1965.

Gabrielli C, Jaouhari R, Joiret S, Maurin G, Rousseau P. Study of the electrochemical deposition of caco[sub 3] by in situ raman spectroscopy. J Electrochem Soc. 2003;150(7):478. https://doi.org/10.1149/1.1579482.

Gal J-Y, Fovet Y, Gache N. Mechanisms of scale formation and carbon dioxide partial pressure influence. Part ii. application in the study of mineral waters of reference. Water Res. 2002;36(3):764–73.

Gal J-Y, Fovet Y, Gache N. Mechanisms of scale formation and carbon dioxide partial pressure influence. Part i. elaboration of an experimental method and a scaling model. Water Res. 2002;36(3):755–63.

Gutjahr A, Dabringhaus H, Lacmann R. Studies of the growth and dissolution kinetics of the $CaCO_3$ polymorphs calcite and aragonite II The influence of divalent cation additives on the growth and dissolution rates. J Crystal Growth. 1996;158(3):310–5.

Heine F, Zosseder K, Einsiedl F. Hydrochemical zoning and chemical evolution of the deep upper jurassic thermal groundwater reservoir using water chemical and environmental isotope data. Water. 2021;13(9):1162. https://doi.org/10.3390/w13091162.

Henry W. Iii experiments on the quantity of gases absorbed by water, at different temperatures, and under different pressures. Philos Trans R Soc. 1803;93:29–43.

Hörbrand T, Baumann T, Moog HC. Validation of hydrogeochemical databases for problems in deep geothermal energy. Geotherm Energy. 2018;6:20. https://doi.org/10.1186/s40517-018-0106-3.

Köhl B, Elsner M, Baumann T. Hydrochemical and operational parameters driving carbonate scale kinetics at geothermal facilities in the bavarian molasse basin. Geothermal Energy. 2020;8:26. https://doi.org/10.1186/s40517-020-00180-x.

Lipus LC, Dobersek D. Influence of magnetic field on the aragonite precipitation. Chem Eng Sci. 2007;62(7):2089–95.

Mayrhofer C, Niessner R, Baumann T. Hydrochemistry and hydrogen sulfide generating processes in the malm aquifer, Bavarian molasse basin, Germany. Hydrogeol J. 2013;22(1):151–62. https://doi.org/10.1007/s10040-013-1064-2.

Morse JW, Arvidson RS, Lüttge A. Calcium carbonate formation and dissolution. Chem Rev. 2007;107:342–81.

Parkhurst DL, Appelo CAJ. Description of Input and Examples for PHREEQC Version 3-A Computer Program for Speciation, Batch-reaction, One-dimensional Transport, and Inverse Geochemical Calculations. US Geol Survey Techn Methods. 2013;6:23.

Plummer LN, Wigley TML, Parkhurst DL. The kinetics of calcite dissolution in CO_2-water systems at 5° c to 60° c and 0.0 to 1.0 atm CO_2. Am J Sci. 1978;278:179–216.

Qian M, Zuo ZY, Chen Y, Liu WY, YangChen Y. Crystallization of $CaCO_3$ in Aqueous Solutions with Extremely High Concentrations of NaCl. Crystals. 2019;9(12):647. https://doi.org/10.3390/cryst9120647.

Sander R. Compilation of Henry's law constants (version 4.0) for water as solvent. Atmos Chem Phys. 2015;15:4399–981.

Sanjuan B, Girard JP. Review of kinetic data on carbonate mineral precipitation. BRGM Report R. 1996;39062:91.

Schröder H, Hesshaus A. Langfristige Betriebssicherheit Geothermischer Anlagen. Bundesanstalt für Geowissenschaften und Rohstofe (BGR). Hannover, Technical report; 2009.

Ueckert M, Baumann T. Hydrochemical aspects of high-temperature aquifer storage in carbonaceous aquifers: evaluation of a field study. Geothermal Energy. 2019;7:1. https://doi.org/10.1186/s40517-019-0120-0.

Ueckert M, Wismeth C, Baumann T. Crystallization of calcium carbonate in a large-scale push–pull heat storage test in the upper jurassic carbonate aquifer. Geothermal Energy. 2020;8:1.

Wanner C, Eichinger F, Jahrfeld T, Diamond LW. Causes of abundant calcite scaling in geothermal wells in the Bavarian molasse basin, southern Germany. Geothermics. 2017;70:324–38. https://doi.org/10.1016/j.geothermics.2017.05.001.

Weber J, Ganz B, Sanner B, Moeck I. Geothermal energy use, country update for Germany. European Geothermal Congress 2016, Strasbourg, France 19-24 September 2016, p. 1–16; 2016.

Wedenig M, Boch R, Leis A, Wagner H, Dietzel M. Green inhibitor performance against $CaCO_3$ scaling: Rate-modeling aided test procedure. Crystal Growth Design. 2021;21(4):1959–71.

Zhang D, Lin Q, Xue N, Zhu P, Wang Z, Wang W, Ji Q, Dong L, Yan K, Wu J, Pan X. The kinetics, thermodynamics and mineral crystallography of $CaCO_3$ precipitation by dissolved organic matter and salinity. Sci Total Environ. 2019;673:546–52. https://doi.org/10.1016/j.scitotenv.2019.04.138.
Zhong S, Mucci A. Calcite and aragonite precipitation from seawater solutions of various salinities: Precipitation rates and overgrowth compositions. Chem Geol. 1989;78:283–99.

Publisher's Note